Numerical study on the cooling characteristics of hybrid thermosyphons: Case study of the Giant Mine, Canada

Article *in* Cold Regions Science and Technology · May 2021

DOI: 10.1016/j.coldregions.2021.103313

Ahmad F. Zueter
McGill University

A.P. Sasmito
McGill University

Numerical study on the cooling characteristics of hybrid thermosyphons: Case study of the Giant Mine, Canada

Ahmad F. Zueter[a], Greg Newman[b], Agus P. Sasmito[a*]

a) Department of Mining and Materials Engineering, McGill University, 3450 University, Frank Dawson Adams Bldg., Montreal, QC H3A0E8, Canada
b) Newmans Geotechnique Inc., 311 Adaskin Cove, Saskatoon SK, S7N 4P3, Canada

Abstract

Hybrid thermosyphons have been installed in several permafrost protection applications due to their ability to operate continuously irrespective of seasonal temperature variations. In winter seasons, the thermosyphon operates passively by transferring energy between the ground and cold ambient air; while in warmer/summer seasons, an active refrigeration plant is used as a substitute for colder climate to extract the heat and freeze the ground. This study presents a novel conjugate mathematical model of hybrid thermosyphons based on thermal resistance networks, coupled with transient two-phase artificial ground freezing heat flow based on the enthalpy method. The model is validated against laboratory experimental data from literature and field test data from the Giant Mine in Yellowknife, Canada. Various design and operating parameters are investigated with the aim to maximizing ground heat extraction while minimizing energy consumption. The results indicate that active refrigeration substantially accelerates the formation of

*Corresponding author.
Email address: agus.sasmito@mcgill.ca (Agus P. Sasmito[a])

the desired frozen ground volume. After a certain time, passive cooling mode can be continuously adopted to reduce the energy consumption of refrigeration plants while maintaining the desired frozen ground thickness. Finally, the model can be used to assist engineers and practitioners to optimize the design of hybrid thermosyphon for permafrost protection or other ground freezing applications.
Keywords: Hybrid thermosyphon, Energy saving, Numerical modeling, Artificial ground freezing, Permafrost regions, Giant Mine.

Nomenclature

Latin letters

A	Area [m^2]
c_p	Specific heat capacity [J kg^{-1} K^{-1}]
f	Friction factor [-]
h	Convective heat transfer coefficient [W m^{-2} K^{-1}]
h_{fg}	Specific latent heat of evaporation [J kg^{-1}]
k	Thermal conductivity [W m^{-1} K^{-1}]
L	Specific latent heat of fusion [J kg^{-1}]
$\dot{m}$	Mass flow rate [kg s^{-1}]
Nu	Nusselt number [-]

Pr Prandtl number [-]

q Heat flux [W m⁻2]

R Thermal resistance [K W^{-1}]

r Radial coordinate [m]

Re Reynolds number [-]

T Temperature [K]

t Time [s]

z Axial coordinate, where $z = 0$ at the top of the domain [m]

Greek letters

δ Frozen ground thickness [m]

γ Liquid fraction [-]

μ Viscosity [Pa s]

ϕ Porosity [-]

ρ Density [kg m^{-3}]

τ Active operation period per year [s]

Subscripts

ℓ Liquid state

a	Air
c	Coolant
e	Evaporator
f	Liquid state
i	Inner wall
n	Condenser
o	Outer wall
r	Rock
s	Saturation state
w	Water, in its frozen or unfrozen states

1. Introduction

The Giant Mine used to be one of the major driving forces of economic growth of the Northwest Territories (Canada) in the second half of the twentieth century [1]. More than 7,000,000 oz of gold were produced from around 20,000,000 tonnes of milled ore [2]. During the production process, the ore was roasted to high temperatures creating more than 237,000 tonnes of highly toxic arsenic trioxide waste [1]. The arsenic waste has been stored in underground chambers and stopes extending from around 20 to 90 meters below ground surface. These chambers and stopes used to be securely surrounded by solid impenetrable permafrost

[3]. Nonetheless, due to global warming and underground activities, permafrost thawing has been intensifying, thereby increasing the risk of arsenic leakage. Consequently, industrial teams initiated the Giant Mine Remediation Project to assess different options of long-term management of the arsenic dust. Ultimately, encapsulating the arsenic waste within an artificially frozen shell was selected due to its construction reliability, robustness, and low risk on the workers and communities [4]. Following that, optimization studies were conducted to test different artificial ground freezing (AGF) techniques. A full-scale field test was developed around one of the smaller arsenic chambers which included conventional ground freezing, passive thermosyphon freezing (e.g. climate only), and hybrid thermosyphon freezing. The field test site was fully instrumented so that a complete understanding of the performance, as well as the capital and operating costs, could be established for each technology. Ultimately, passive thermosyphons with an optional conversion to hybrid cooling have been selected and construction will commence in 2021.

In addition to the Giant Mine, several AGF applications have tested and installed hybrid thermosyphon technologies. The first commercial use of this technology dates back to 1984 in Galena, Alaska, where it was used to freeze and stabilize the foundations of a communication site [5, 6]. Perhaps a more notable application of hybrid thermosyphons was the containment of contaminated water at the Oak Ridge National project in 1997 [7, 8]. In this case, fifty hybrid thermosyphons were used to create a frozen wall preventing the leakage of radionuclides rich water. More recently, hybrid thermosyphons have been widely used in civil and mining applications in Canada. For example, they have been employed to speed up ground freezing for earlier construction of the Inuvik Hospital (Northwest Territories, Canada), to increase the efficiency of partially damaged passive thermosyphons of the Female Young Offender Facility (Northwest Territories, Canada), and to protect frozen ground affected by heat supply lines at the Simon Allaituq School (Nunavut, Canada) [9]. In the mining industry, the Diavik Diamond Mine (Northwest Territories, Canada) installed hybrid thermosyphons to accelerate the ground freezing associated with the construction of the mine dams [10] and the Lac De Gras dikes [9]. Furthermore, it is reported that hybrid thermosyphons are being employed more frequently in Russia [11]. In general, hybrid thermosyphons are attracting a widespread interest in the fields of AGF and permafrost protection because of their high operational adaptability to different ground and weather conditions.

A hybrid thermosyphon is made of a conventional refrigerant filled thermosyphon with the addition of a hybrid mechanical cooling unit as as shown in Fig. 1. They feature two types of condensers: an active condenser and passive condensers. Active condensers require a refrigeration system to supply a low temperature coolant during warm seasons, as shown in Fig. 1(a). This coolant is pumped through a helical coil to condense the refrigerant and extract its heat. On the other hand, passive condensers are equipped with radiator fins which exploit the cooling capacity of the ambient air during cold seasons to extract heat from the refrigerant, as can be seen from Fig. 1(b). In addition to the two condenser sections, hybrid thermosyphons comprise an evaporator section embedded in the ground. Overall, the thermosyphon operation is a multi-scale and multi-physics problem.

Accordingly, many mathematical studies have investigated *passive* cooling of thermosyphons in AGF applications. Yang et al., Lu et al., and Duan et al. [12, 13, 14] built mathematical models based on fields measurements to evaluate heat absorption by thermosyphons. To the best of our knowledge, the first to develop a coupled thermal resistance model of passive thermosyphons for AGF applications is Yang et al. [15, 16, 17] in 1998, in attempts to monitoring the freezing expansion of soil in the vicinity of construction foundations. Their model discretized the ground in 2D cylindrical co-ordinates and included the thermal resistance of the wind, condenser wall, liquid film condensation, liquid film boiling, pool boiling, and evaporator wall, as can be depicted from Fig. 2(a). Zhi et al. [18], Xu et al. [19], and Abdalla et al. [20, 21] simplified the thermal resistance network by considering a superconductor thermosyphon, linking the ambient air temperature with the outer wall temperature of the evaporator by a single thermal resistance located between the ambient air and the condenser, as shown in Fig. 2(b). Nevertheless, they added a switch, S_1, to deactivate the natural convection cycle of the thermosyphon when the evaporator temperature is lower than the condenser temperature; In addition, a 3D numerical model for the ground was considered. Wang et al. and Tian et al. [22, 23] assumed a similar superconductor thermal resistance model, but selected Nusselt correlations that depended on the wind velocity in their calculation of the wind thermal resistance. In 2011, Zhang et al. [24] used a 3D numerical model while extending the thermal resistance model by including the conduction, evaporation, and condensation thermal resistances inside the thermosyphon in addition to the S_1 switch and wind thermal resistance, as shown in Fig. 2(c). Film and pool boiling regimes were modeled by a single Nusselt correlation [25] applicable to both regimes. Since then, this 3D thermal resistance model has been used by many researchers to investigate passive cooling of thermosyphons for AGF applications [26, 27, 28, 29, 30]. Recently, Pei et al. [31, 32] firstly considered the inclination angle of the thermosyphon by modifying the evaporation and condensation correlations.

While there is a considerable amount of literature on passive thermosyphons [33, 34, 35, 36, 37] and conventional freeze-pipes [38, 39, 40, 41, 42], few studies have considered hybrid thermosyphons as an AGF technique. Haynes et al. [43] performed a series of experiments on hybrid thermosyphons to study the effects of the coolant inlet temperature and flow rate on the equivalent thermal conductance of hybrid thermosyphons. The maximum inlet temperature and minimum inlet flow rate of the coolant were found to be -16 [°C] and 0.24 [kg s^{-1}], respectively, to obtain an equivalent thermal conductance of 3 [W $m^{-1}K^{-1}$] or greater — which is considered adequate for most foundation stabilization applications in Alaska [43]. Wagner and Yarmak [44, 45] investigated the quickness of frozen barrier formation by conducting several tests in Alaska. The frozen body thickness reached to 1 [m] during the active operation in the summer which lasted for 60 days, and then extended to 3.8 [m] during the passive operation in the winter season.

Previous work on hybrid thermosyphon technologies of AGF applications is limited to the experimental level. Nevertheless, there is a need for mathematical modeling of these technologies to better understand the underlying physics of their operation and thereby improve their performance in the field. As a consequence, the aim of our work is to develop a reliable coupled heat transfer model of hybrid thermosyphons. To this end, a thermal resistance model will be developed and validated against experimental measurements from the literature and field data from the Giant Mine technical reports [3, 46]. The model will be then employed to study the influence of various operational parameters on the performance of hybrid thermosyphons, namely the frozen ground expansion and the cooling load of refrigeration plants.

The paper is organized as follows. First, the mathematical model is presented, including a detailed derivation of the thermal resistance model of hybrid thermosyphons. After that, the model is validated against experimental measurements from the literature and field data from the Giant Mine tests. Finally, a set of parametric studies are conducted to analyze the design of hybrid thermosyphons

2. Mathematical model formulation

In this section, the governing equations and boundary conditions of the hybrid thermosyphon model are presented.

2.1. Governing equations

The computational domain of the present study is made up of the ground, a porous medium that consists of rock and water. Throughout this study, the saturated porosity of the ground does not exceed 10%, and the thermophysical properties of the rock and water are very close to that of the experimental study of Zueter et al. [39]. For this range of properties, Zueter et al. [39] determined that the local thermal equilibrium (LTE) assumption [47] is valid. Energy conservation in the ground can thus be expressed by balancing the diffusive and transient terms of the temperature field considering a one-temperature model as

$$\frac{\partial(\overline{\rho c_p}T)}{\partial t} = \nabla \cdot (\bar{k}\nabla T) + S, \tag{1}$$

where $\overline{\rho c_p}$ and $\bar{k}$ are the equivalent heat capacity and thermal conductivity of the ground (rock and water), while the source term, S, is added to include the latent heat of the water and is expressed as

$$S = -\frac{\partial(\gamma\overline{\rho L})}{\partial t}, \tag{2}$$

where $\overline{\rho L}$ is the equivalent volumetric latent heat of the ground and γ is the liquid fraction calculated based on the temperature as

$$\gamma = \begin{cases} 0 & , T < T_{sol}; \\ \frac{T - T_{sol}}{T_{liq} - T_{sol}} & , T_{sol} \leq T \leq T_{liq}; \\ 1 & , T > T_{liq}, \end{cases} \tag{3}$$

where T_{sol} and T_{liq} denote the solidus and liquidus temperatures, respectively. The equivalent latent heat content is related to the ground porosity, ϕ, as

$$\overline{\rho L} = \phi \rho_w L_w, \tag{4}$$

where ρ_w and L_w are the density and latent heat of water, respectively.

2.2. Boundary conditions

The thermosyphon boundary condition is the source of heat extraction from the ground and will therefore be analyzed separately in Section 2.2.1. After that, mathematical modeling of the other boundaries will be presented in Section 2.2.2.

2.2.1. Hybrid thermosyphon boundary condition

The thermosyphon boundary condition is modeled with the aid of a thermal resistance network, as shown in Fig. 2(d) and listed below:

1. Evaporator wall (R_1): The conductive thermal resistance of the evaporator wall, R_1, is given as [48]

$$R_1 = \frac{1}{2\pi k_{steel} \ell_e} ln\Big(\frac{D_{o,e}}{D_{i,e}}\Big), \tag{5}$$

   where k_{steel}, ℓ_e, $D_{o,e}$, and $D_{i,e}$ are the thermal conductivity of steel, length of the evaporator section, outer diameter of the evaporator wall, and inner diameter of the evaporator wall, respectively.

2. Liquid film and pool boiling ($R_{2,3}$): Immura's correlation [25] for the heat transfer coefficient of combined liquid film and pool boiling is adapted in

this study as it has been employed and verified in multiple studies [49, 50]. The overall heat transfer coefficient is expressed as

$$h_{2,3} = 0.32\left[\frac{\rho_f^{0.65} k_f^{0.3} c_{p,f}^{0.7} g^{0.2} q_e^{0.4}}{\rho_g^{0.25} h_{fg}^{0.4} \mu_f^{0.1}}\right]\left(\frac{P_s}{P_{atm}}\right)^{0.3} \tag{6}$$

where g, μ, h_{fg}, and P_{atm} are the gravitational acceleration, viscosity, latent heat of vaporization, and atmospheric pressure, respectively. The subscripts f, g, and s refer to the liquid, gas, and saturated state of the refrigerant inside the thermosyphon. The overall boiling thermal resistance, $R_{2,3}$, can now be determined as

$$R_{2,3} = \frac{1}{h_{2,3} A_{i,e}}, \tag{7}$$

where $A_{i,e}$ is the area of inner wall of the evaporator section.

3. Film condensation (R_4): The heat transfer coefficient correlation derived by Nusselt [51] is selected due to its agreement with the laminar flow regime of this study, as well as its frequent reliability [52]. The film condensation heat transfer coefficient is given as

$$h_4 = 0.925\left[\frac{k_f^3 \rho_f^2 g h_{fg}}{\mu_f q_n \ell_n}\right]^{1/3}. \tag{8}$$

where q_n is the heat flux through the condenser while L_n is the length of the condenser. The condensation thermal resistance can then be calculated as

$$R_4 = \frac{1}{h_4 A_{i,n}}, \tag{9}$$

where $A_{i,n}$ is the area of the inner side wall of the condenser.

4. Condenser wall (R_5): The conductive thermal resistance of the condenser wall is given as [48]

$$R_5 = \frac{1}{2\pi k_{steel}\ell_n} ln\Big(\frac{D_{o,n}}{D_{i,n}}\Big), \tag{10}$$

where $D_{o,n}$ and $D_{i,n}$ are the height of the condenser section, the outer diameter of the condenser wall, and the inner diameter of the condenser wall, respectively.

5. Air-fin (R_6): The Nusselt number of air flow across the condenser relies on the Reynolds number of the wind, Re_a, as [48, 53]

$$Nu_a = \frac{h_6 D_{o,c}}{k_a} = \begin{cases} \eta_{fin}\ 0.989 Re_a^{0.330} Pr_a^{1/3} & ,\ Re_a < 4; \\ \eta_{fin}\ 0.911 Re_a^{0.385} Pr_a^{1/3} & ,\ 4 \leq Re_a < 40; \\ \eta_{fin}\ 0.683 Re_a^{0.466} Pr_a^{1/3} & ,\ 40 \leq Re_a < 4000; \\ \eta_{fin}\ 0.193 Re_a^{0.618} Pr_a^{1/3} & ,\ 4000 \leq Re_a < 40000; \\ \eta_{fin}\ 0.027 Re_a^{0.805} Pr_a^{1/3} & ,\ 40000 \leq Re_a, \end{cases} \tag{11}$$

where η_{fin} is the fin efficiency, which is a function of the fin geometry and determined to be 65% according to the charts of Gardner [54, 48] for circular fins. The thermal resistance of the air flow across the condenser can now be calculated as

$$R_6 = \frac{1}{h_6 A_{fin}}, \tag{12}$$

where A_{fin} is the finned area of the condenser. Heat convection from the unfinned part is neglected due to its small contribution in the heat transfer as compared with the finned part.

6. coil-condenser (R_7): In hybrid thermosyphons, helical coils are compactly wrapped around the active condenser region. Active cooling is achieved by pumping a refrigerated liquid into these coils to condense the refrigerant and force the thermosyphon evaporation/condensation cycle. These coils are well insulated to maximize heat extraction from the condenser and minimize heat gain from the ambient air to the coolant. Heat transfer efficiency between such insulated coils and thermosyphons, η_{hc}, is assumed to be 90% as measured experimentally by Wang et al. [55].

   The Nusselt number correlation proposed by Seban and Mclanghin [56, 57] is adapted as its range of Reynolds number, Prandtl number, and Deans number is within the limits of our study. This correlation is expressed as

$$Nu = \frac{h_7 D_c}{k_c} = 0.065 f_c^{0.33} Re_c^{0.66} Pr_c^{0.33}, \tag{13}$$

   where f_c is the friction factor of the coolant flow calculated as [58]

$$f_c = \frac{64}{Re_c}\left\{1 - \left[1 - \left(\frac{11.6}{Dn_c}\right)\right]^{0.45}\right\}^{-1} \tag{14}$$

   where Dn_c is the Deans number. The thermal resistance of the helical coils can then be calculated as

$$R_7 = \frac{1}{\eta_{hc} h_7 A_c}, \tag{15}$$

where A_c is the heat transfer area of the coils.

After calculating each individual thermal resistance, the equivalent thermal resistance is determined. The evaluation of the equivalent thermal resistance depends on the status of the three switches shown in Fig. 2. S_2 and S_3 are user-controlled representing active and passive cooling regimes. During passive operations in cold seasons, S_3 is switched on to activate passive cooling while S_2 is switched off indicating that the refrigeration plant is inactive. On the other hand, during warm seasons, S_3 is switched off while S_2 is switched on. The coils are often designed to be large enough to ensure that the refrigerant condenses in the active condenser section before reaching the passive condensers. Unlike S_2 and S_3, S_1 is not user-controlled; it represents the status of the natural convection cycle of the refrigerant inside the thermosyphon. Particularly this switch is opened only when the heat sink temperature (air or coolant temperature) is higher than that of the evaporator wall temperature.

Once the equivalent thermal resistance, R_{eq}, is found, the equivalent heat flux across the evaporator wall, q_e, can be determined as

$$q_e = \frac{Q_{total}}{A_e} = \frac{T_\infty - T_e}{R_{eq} A_e}, \tag{16}$$

where subscript e refers to the outer evaporator wall, and T_∞ represents the heat sink temperature. The thermal boundary condition along the evaporator wall can then be expressed as

$$-\bar{k}\frac{\partial T}{\partial n}\bigg|_e = q_e, \tag{17}$$

where n is a normal vector to the boundary.

2.2.2. Ground boundary conditions

In addition to the hybrid thermosyphon boundary, other boundary conditions are mathematically modeled. An axi-symmetric boundary is set in most of the simulations where the variations of the temperature field in the angular direction is negligible as compared with that of the radial and axial directions. This boundary is often considered in simulations that involve a single thermosyphon in an axi-symmetric computational domain. In these simulations, the change of temperature in the radial direction equals to zero along the axis of symmetry as [48]

$$\left.\frac{\partial T}{\partial r}\right|_{axis} = 0. \tag{18}$$

Along the bottom boundary, geothermal heat flux is set as [48]

$$-\bar{k}\left.\frac{\partial T}{\partial n}\right|_{bottom\ boundary} = q_{geo}, \tag{19}$$

where $q_{geo} = 0.06$ [W/m^2].

Boundary independence study was conducted at the far boundary from the evaporator to ensure that this boundary has no effect on the temperature field near the thermosyphon. The study shows that a distance of 50 [m] is sufficient to obtain a boundary independent solution. The far boundary is an insulated wall as

$$\left.\frac{\partial T}{\partial n}\right|_{far\ boundary} = 0. \tag{20}$$

The top boundary of field simulations is subject to atmospheric convection as

$$-\bar{k}\frac{\partial T}{\partial n}\bigg|_{top\ boundary} = h(T|_{top\ boundary} - T_a), \tag{21}$$

where T_a is the air temperature and the atmospheric heat transfer coefficient is set at 3 [W/(m^{2}K)].

3. Choice of numerical parameters

The spatial and transient terms of the governing equation of the ground (Eq. (1)) were discretized by second order upwind schemes. The non-linear equations of the thermal resistance network model were solved inside a set of user-defined-functions (UDF) iteratively, in conjunction with the iterative solution of the governing equations of the ground and other boundary conditions listed in Section 2.2.2. ANSYS Fluent 18.1 was used to compute the equations as prescribed by our model and UDFs.

Prior to validating our model and running the parametric studies, mesh independence study was conducted and ensured. The selected mesh size and type greatly relies on the simulation scenario as we have conducted various 3D and 2D simulations of different length scales. In all cases, the mesh and geometry were generated with the aid of ANSYS Fluent 18.1.

4. Validation

The model was validated in three consecutive stages. First, the passive cooling regime was validated against an experimental study from the literature [59]. After that, this passive model was extended to field scale and validated against field data from the Giant Mine test study [3]. Lastly, the active cooling regime was incorporated to the passive cooling model, and the combined model was validated against field data from the Giant Mine freezing optimization study (FOS) [46].

4.1. Passive cooling validation against an experimental study

Mathematical modeling of the passive cooling mode was validated against the experimental study of Pei et al. [59]. The experimental setup consisted of a thermosyphon filled by ammonia, a 9.8% porous soil, and fans, as shown in Fig. 3. Prior to starting the experiment, the soil temperature was uniformly set at 16 [°C] as recorded by multiple thermocouples. After that, air was blown by a fan for 72 hours at a speed of 2.8 m/s and a sinusoidal temperature of

$$T[^{\circ}C] = -12\ sin\left(\frac{2\pi}{216}\ t[hr]\right). \tag{22}$$

The transient temperature data of three thermocouples, shown in Fig. 3, were reported. More details about the experiment can be found in [59].

Very good agreement is noted between the results of our mathematical model and the experimental measurements, as shown in Fig. 4. The sinusoidal behavior of the temperature profile is caused by the sinusoidal variation of the air temperature, as noted from Eq. 22. The thermosyphon extracts heat from the ground when the air temperature is lower than the evaporator temperature, resulting in reduction of ground temperature. Nevertheless, as the thermosyphon is inactive when the air temperature is higher than the evaporator wall temperature (S_1 opens), the temperature of the ground near the thermosyphon increases due to the incoming heat from the surrounding warmer ground. The small time lag between the numerical results and the experimental data of the ground temperature is attributed to the uncertainty of the thermal diffusivity of the sand and exact phase change temperature of the water content.

4.2. Passive cooling validation against the Giant Mine field test study

Although thermosyphons have been used in the AGF industry for many decades prior to the Giant Mine Remediation Project, most of the applications have thermosyphons installed closer to the ground surface. However, the arsenic chambers which need to be frozen at the Giant Mine are 75 meters deep with one extra zone requiring thermosyphons to be 140m deep. For this reason, a preliminary experimental study was initiated at the Giant Mine in 2002 to ensure the capability of thermosyphons to extract heat over longer depths.

The field experiment involved a 102.1[m] deep thermosyphon (refer to Table 1 for details on the geometry [60]) embedded in layered ground. Specifically, the top five meters of the ground was overburden (clay and silt mixture), sitting above bedrock (greenstone). The thermosyphon was charged by pressurized carbon dioxide rather than ammonia since the latter tends to form non-condensable gases that occupy significant portions of the condenser and thereby reduce the condenser efficiency. In addition, ammonia was avoided since it poses significant health and safety risks on the workers. The thermophysical properties of the overburden, bedrock, and carbon dioxide are listed in Table 2. Approximately 20 thermocouples were fixed either directly to the outer wall of the evaporator to monitor heat transfer across the ground-pipe contact, or within an adjacent instrumentation hole to monitor cooling in the ground. This hole was originally targeted to be 2 meters away from the thermosyphon, but vertical alignment survey revealed that the distance between the thermosyphon and the thermocouples ranges between 2.1 [m] and 2.8 [m], as shown in Fig. 6(a). After completing the installation, the field experiment started on the fifth of March 2002, and the initial results were reported on the third of May 2002. The temperatures of the ground and evaporator wall in these two dates were measured, as shown in Fig. 6(b) and Fig. 6(c), respectively.

The accuracy of our mathematical model was tested against the field data measurements. The air temperature and speed data were not averaged (curve-fitted) as Fong et al. [61] found that heat transfer calculations are highly influenced by the instantaneous variations of environmental data. Instead, hourly data measured by the Giant Mine weather station [62] were adopted in this study, as shown in Fig. 5. The results demonstrated the ability of the mathematical model to anticipate the evaporator and ground temperatures in field dimensions. The temperature of the ground 5 meters below the surface is noted to be slightly warmer than that of 10 meters below the surface due to the presence of the highly porous overburden at the top. The significance of layered ground modeling is studied in detail by

Zhou et al. [63]. Overall, the ground temperature decreased by around 0.5 [°C] throughout the depth of the thermosyphon. Such a small difference in temperature is expected since only a single thermosyphon was operated during relatively warm months (as compared to winter seasons) and for a short period of time. Still, this study successfully achieved its primary objective of operating deep thermosyphons in AGF applications.

4.3. Hybrid cooling validation against the Giant Mine field data

Following the success of deep lone thermosyphons test, the freezing performance of multiple AGF techniques were investigated at full field scale around the perimeter of one of the smaller arsenic chambers, as shown in Fig. 7. From this study, we have selected group F to validate our hybrid thermosyphon model. This group includes four hybrid thermosyphons and three instrumentation holes as shown in Fig. 7. The thermosyphons were initially set on the passive cooling mode from the 5^{th} of March 2011 till the 25^{th} of May 2011, as noted from Fig. 8(a). From this date onward, active cooling mode was adopted for a period of around 7 months. A type of hydrocarbon refrigerants called R-507 was chosen to be the coolant of the active cooling regime because of its environmentally friendly and non-corrosive qualities. The geometry of the hybrid thermosyphons and the thermophysical properties of R-507 [64] can be found in Table 3 and Table 2, respectively.

The results of our mathematical model are in a good agreement with the field measurements, as can be seen from Fig. 8(b). During passive operation, the heat flux fluctuated due to the hourly variation of the wind temperature and speed. By the end of the passive operation, the air temperature became warmer than the evaporator temperature. Consequently the natural convection cycle inside the thermosyphon stopped, cutting the heat transfer circuit (the S_1 switch shown in Fig. 2(d) is opened) and resulting in a zero heat flux. This led to an increase in the ground temperature by the end of the passive regime. Once active operation is switched on (S_2 is closed), the heat flux significantly increased, and the ground freezing process resumed. The results also show that the ground temperature dropped faster in the active cooling mode as compared with the passive one. This would be the case of such hybrid thermosyphons using coolants running at low temperatures (around -35 [°C]) and high flow rates (20-100 [kg/hr]). The small deviations of the third instrumentation hole is likely due to the spatial variations of the water content of the bedrock especially near the chamber.

5. Results and discussion

In this section, the frozen ground development and cooling load of hybrid thermosyphons are investigated. First, the change of the frozen ground profile is analyzed for a period of two years. After that, the impact of various parameters are investigated to understand and optimize hybrid thermosyphons.

5.1. Year-round frozen barrier profile

The extent of the frozen ground profile was tracked on a monthly basis for two years, as shown in Fig. 9. Active cooling was switched on during warmer seasons from the 15th April till the 15th of October, thereby operating the thermosyphon actively six months a year.

In the first year, the frozen ground extents increased for two months due to the colder climate in January and February. The positive slope of the phase transition front was caused by the geothermal gradient of the initial condition. In March, the air temperature increased which significantly decreased heat extraction by the thermosyphon; consequently, the frozen ground shrank due to heat gain from the underlying and surrounding ground. By the end of April, the frozen ground expanded again as active cooling was activated on the 15th April. In the following months, though the active layer (few meters deep from ground surface) thawed due to the warm air, the frozen body continued to dilate as long as active cooling was operated until the middle of October.

By the end of October, the frozen ground extent slightly decreased since active cooling was switched off. Despite the cold wind temperature of the winter season, the frozen ground tended to contract throughout the passive operation in the second year. This could be understood by conducting a simple energy balance on the frozen ground based on the first law of thermodynamics:

$$\dot{E}_f = \dot{E}_{in} - \dot{E}_{out} = \dot{E}_r - \dot{E}_t - \dot{E}_s \tag{23}$$

where $\dot{E}_f$ is the transient change of energy of the frozen ground, $\dot{E}_r$ is the rate of incoming heat from surrounding unfrozen rocks, $\dot{E}_t$ is the rate of heat extraction of the thermosyphon during passive operation, and $\dot{E}_s$ is heat extraction/addition from the ground surface. The decline of frozen ground size correlates to a positive $\dot{E}_f$ indicating that energy added by the surrounding unfrozen rocks is higher than that extracted by the thermosyphon. This is primarily attributed to the very low temperature of the frozen ground following the active operation due to the low coolant temperature (-30 [°C]). Nonetheless, after switching on active cooling again in the middle of April of the second year, the frozen ground expanded again in a similar manner of that of the first year.

In the second year, the extent of the frozen ground is larger at a depth of 10 meters than on the ground surface even during winters seasons. This indicates that the cold energy absorbed by the ground surface (top few meters) in the first year was lost due to the summer season heating. On the other hand, the deeper portion of the ground stores the cold energy more effectively since it is away from the ground surface. At these deeper levels, the cold energy is lost to the warmer surrounding ground only which is much less significant than seasonal ground thawing observed on the surface.

5.2. Parametric analysis

In this section, we will study the impact of different operational parameters of hybrid thermosyphons on the frozen ground expansion and the heat extracted by hybrid thermosyphons in passive and active modes.

5.2.1. Coolant temperature

Reducing the coolant temperature enlarged the frozen ground even during winter seasons when active cooling was switched off, as shown in Fig.10. This implies that the benefits of active cooling are still realized throughout the year despite its intermittent operation. Nonetheless, the transient expansion rate of the frozen ground volume lessened as the coolant temperature is reduced, even though decreasing the coolant temperature resulted in a linearly proportional increase in the cooling load of active freezing plants, as noted in Table 4. For example, by examining winter-time subplots of the first and second years shown in Fig. 10, the radius of the frozen ground at a depth of 50 meters expands by 67%, 60%, and 50% at coolant temperatures of -20 [°C], -30 [°C], and -40 [°C], respectively. This observation indicates that lower coolant temperature consumed more energy to over-cool the frozen ground. Accordingly, it might be desirable to intensively reduce the coolant temperature (e.g., -40 [°C]) in early stages of operation to speed up the freezing process, but then increase the coolant temperature in subsequent years to reduce the cooling load.

5.2.2. Coolant flow rate

At the Giant Mine freeze study, a high coolant flow rate was often considered to exist between 20 [kg/hr] to 100 [kg/hr], in order to ensure that the coolant continued to extract heat throughout the length of the helical coil. Increasing the coolant flow rate resulted in higher Reynolds number and Nusselt number, as can be noted from Eq. (13). Since the Nusselt number is inversely proportional to the thermal resistance of the flow (R_7), heat extracted is higher at larger flow rates, leading to a larger frozen ground as shown in Fig. 11. Specifically, after two years of operation, the extent of frozen ground at a flow rate of 100 [kg/hr] was larger by 7% and 25% as compared to that of 60 [kg/hr] and 20 [kg/hr], respectively (these percentages are calculated at a depth of 50 meters). Nevertheless, as more heat was extracted at higher flow rates, the resulting cooling load was higher, as mentioned in Table 4.

5.2.3. Active cooling operation period

In the Giant mine, the coolant often runs at low temperature of around -35 [°C] and high flow rates of around 60 [kg/hr]. Active cooling is therefore usually larger than passive cooling despite the cold temperature of the ambient air, as demonstrated in Fig. 8. A larger frozen ground is therefore expected as the active cooling operation period, τ, increases, as shown in Fig. 12. Specifically, the frozen ground radius at a depth of 50 meters increased by 30.9% and 63.9% when τ was increased from 4 months to 6 months and 8 months, respectively. Longer τ however indicates that the refrigeration plants were operated for a longer time. Accordingly, the cooling load almost doubled when τ was increased from 4 months to 8 months, as noted in Table 4. Although the passive operational period at $\tau = 4$ [mo.] is twice as long as that of $\tau = 8$ [mo.], the increase in passive energy extraction amounts to 25% only after two years of operation. This is attributed to the warm air temperature in the spring and fall seasons, causing the thermosyphon to be almost idle for around 3 months per year as implied by Fig. 13(b).

In reality, several hybrid thermosyphon applications involve a series of adjacent thermosyphons working together, rather than a single thermosyphon, to create a frozen barrier, as shown in Fig. 13(a). The spacing between them is designed according to the desired duration to reach a particular δ, which is the laterally outward frozen ground thickness from the row of the pipes as shown in Fig. 13(a). In other words, freezing needs to continue until a minimum desired δ is reached. Assuming the desired δ to be 6[m], running the thermosyphons actively for 8 months (τ = 8 [mo.]) could achieve this objective in 4.5 months, as can be seen from Fig. 13(c). Similarly, when τ = 4 [mo.], 6.5 months were needed to obtain δ = 6[m]. On the other hand, if the thermosyphons were operated passively only without the use of mechanical refrigeration, δ would extend to 6 [m] after more than two years. Evidently, adding mechanical refrigeration units to the thermosyphon substantially speed up the freezing process.

Once the desired δ is reached, active cooling units may no longer be needed especially in arctic regions, where the ambient air temperature is low enough to effectively operate the thermosyphon passively. Fig. 13(c) shows that passive cooling is sufficient to maintain the desired δ after around two years of operation even if it was not preceded by active cooling. This observation is important as maintaining long active operation period for long lasting AGF systems, such as the arsenic containment of the Giant Mine, can result in additional cooling load of around 20 [MWh] per year per thermosyphon, as can be seen from Fig. 14(a). Furthermore, the evaporator wall temperature becomes very low after few years of operation resulting in a significant decrease during passive heat extraction at longer τ, as shown in Fig. 14(b). Consequently, in the case of the Giant Mine, active cooling would be needed in the early stages to accelerate the formation of the desired frozen ground in the first year, but the cold ambient temperature could be reliably utilized to passively run the thermosyphon and maintain the desired frozen body thickness without running refrigeration plants in the following years.

5.2.4. *Helical coil curvature ratio*

The curvature ratio, R^*, of the helical coil is defined as the radius of the thermosyphon divided by the radius of the helical coil. In this subsection, the curvature ratio of the coil was changed from 5 to 15 by changing the coil diameter given the same coil height and thermosyphon diameter. Increasing the curvature ratio enhances the active freezing process as can be depicted from Fig. 15. This is attributed to the higher Reynolds number and thereby heat transfer coefficient of the coolant flow at larger curvature ratios. Particularly, the heat transfer coefficient rises from 42 [W/m^{2}k] at $R^* = 5$ to 236 [W/m^{2}k] at $R^* = 15$. The higher heat extraction at larger R^* resulted in larger cooling load as can be seen from Table 4. Despite the enhanced heat extraction at higher curvature ratios, increasing R^* led to a longer coil which may increase the overall coolant temperature (depending on the mass flow rate) and accordingly reduce heat extraction from the ground. Thus, these results may somewhat overestimate the enhancement of heat extraction at higher curvature ratios, especially at low mass flow rate.

5.2.5. *Number of helical coils*

Varying the number of helical coils was one of the design concerns of hybrid thermosyphons in the Giant Mine FOS. For this reason, field testing was conducted with single-coil thermosyphons and double-coil thermosyphons. It was observed that a double-coil thermosyphon had a similar thermal effect on the ground as that of a single-coil thermosyphon.

The results of the present study agree with the field observations. As can be seen from Fig. 16, the frozen ground of a double-coil thermosyphon was larger by only few centimeters than that of a single-coil thermosyphon. while marginal increase was caused by the larger surface area of a double-coil thermosyphon, a significant enhancement on the freezing rate would not be possible since heat conduction from the ground is slower than heat convection of the coils. However, the influence of doubling the number of coils could be larger if shorter coils are considered or if the length of the evaporator piping is extended.

6. Conclusion

A hybrid thermosyphon is an artificial ground freezing (AGF) technique that balances climate induced cooling, mechanical cooling and ground heat extraction. During cold seasons, hybrid thermosyphons operate passively by taking advantage of the cold air temperature; nonetheless, during warm seasons, they run actively with the aid of refrigeration plants, which refrigerate a coolant that flows around the thermosyphon through a helical coil. In this study, a new mathematical model of hybrid thermosyphons has been developed for ground freezing applications. Particularly, a conjugate thermal resistance network model was derived to find the net heat flux extracted by a hybrid thermosyphon. The equivalent heat flux in the condenser section of a thermosyphon was then applied to the ground heat extraction, which is itself modeled by a two-phase transient energy conservation equation. This conjugate model was firstly validated against experimental measurements from the literature. After that, the model was extended to field dimensions and then further validated against field data from the Giant Mine preliminary tests and freeze optimization studies.

Following the validation of our thermal resistance model, a set of parametric studies were carried out to analyze and optimize the operational parameters of hybrid AGF systems. First, decreasing the coolant temperature and increasing the coolant flow rate enlarged the frozen ground, but decreasing the coolant temperature to below -30 [°C] resulted in overcooling the frozen ground at the cost of unnecessary energy consumption. Second, increasing active operation period might be desired in the first year of operation; however, shorter operation periods (around 3 months) or fully passive operation can maintain the targeted frozen ground in the following years with a lesser energy consumption. Third, doubling the number of coils does not provide significant freezing advantage for the evaporator pipe lengths considered here, especially if long coils (more than 2 meters high) are selected. Lastly, the cooling rate of thermosyphons is highly influenced by the curvature ratio of the coils (helical coil curvature diameter divided by the coil diameter); particularly, tripling the curvature ratio from 5 to 15 increased the heat transfer coefficient of the coil by one order of magnitude, from 42 [W/(m^2K)] to 236 [W/(m^2K)].

In our future work, we aim to improve the applied and fundamental aspects of this work. We will propose an innovative cold energy storage technology that minimizes the need for refrigeration plants. Further, we aim to find the optimal combination of operational parameters to obtain the optimum frozen ground thickness based on the energy consumption for the Giant Mine.

Acknowledgments

The authors would like to thank the FRQNT Development Durable du Secteur Minier – II (2020-MN-284402), Ultra Deep Mining Network (UDMN) (241695 Tri-Council (NCE – UDMN) 2-003). The first author wishes to thank the McGill Engineering Doctoral Award (MEDA).

References

[1] Government of Canada, History of Giant Mine (2018).
URL https://www.aadnc-aandc.gc.ca/

[2] R. Silke, The Operational History of Mines in the Northwest Territories, Canada, Tech. rep., Yellowknife (2009).

[3] Steffen Robertson and Kirsten (Canada) Inc., Giant Mine Ground Freezing, Tech. rep., Vancouver (2002).

[4] Government of Canada, The Remediation Project's Frozen Block Method (2018).
URL www.aadnc-aandc.gc.ca

[5] E. Yarmak, E. L. Long, Recent developments in thermosyphon technology, in: Cold Regions Engineering: Cold Regions Impacts on Transportation and Infrastructure, Anchorage, 2002, pp. 656–662.

[6] E. L. Long, E. Yarmak, Engineering and economic variables of long duration frozen barriers, in: International Symposium on Ground Freezing and Frost Action in Soils, Louvain-la-Neuve, 2000, pp. 169–173.

[7] S. W. Lynn, S. Rock, C. Rhodes, Evaluation of a vertical frozen soil barrier at oak ridge national laboratory, Remediation 10 (3) (2000) 15–33.

[8] E. Yarmak, Permafrost foundations thermally stabilized using thermosyphons, in: Offshore Technology Conference, Copenhagen, 2015, pp. 639–650.

[9] I. Holubec, Flat loop thermosyphon foundations in warm permafrost, Tech. rep., I. Holubec Consulting Inc., Northwest Territories (2008).

[10] Indian and Northern Affairs of Canada, Giant Mine Remediation Project: Developer's Assessment Report - Environmental Assessment, Tech. Rep. October, Northwest Territories (2010).

[11] A. Wagner, Review of Thermosyphon Applications, Tech. rep., US Army Corps of Engineers, Hanover (2014).

[12] Y.-P. Yang, S.-H. Zhou, Q.-C. Wei, Numerical Analysis of Proper Thermosyphon Inclination Angle Used in Permafrost Embankment, China Railway Science 27 (3) (2006) 1–7.

[13] G.-F. Lu, Y.-P. Yang, Q.-C. Wei, L.-X. Zhang, Study of using thermosyphon-insulated board to enhance the stability of permafrost embankment, Journal of the China Railway Society 29 (6) (2007) 118–122.

[14] D. Duan, Y. Yang, Q. Wei, L. Zhang, Study on enhancing the stability of permafrost embankments with thermosyphon-insulated boards, Journal of Beijing Jiaotong University 32 (1) (2008) 24–28.

[15] P. Yang, Numerical Analysis and Application Research of Heat Pipe to Solve Soil Frost Heaving Problem, Journal of East China Jiaotong University 15 (4).

[16] W. Cunzhen, S. Zhijian, P. Yang, Theoritic study on the technology of applying heat pipe to solving frost heaving, Chinese Journal of Geotechnical Engineering 24 (3) (2002) 347–350.

[17] P. Yang, W. Cunzhen, Numerical investigations and engineering applications on freezing expansion of soil restrained two-phase closed thermosyphons, International Journal of Thermal Sciences 41 (4) (2002) 341–347.

[18] W. Zhi, S. Yu, M. Wei, Q. Jilin, J. C. Wu, Z. Wen, Y. Sheng, W. Ma, J. L. Qi, J. C. Wu, Analysis on effect of permafrost protection by two-phase closed thermosyphon and insulation jointly in permafrost regions, Cold Regions Science and Technology 43 (3) (2005) 150–163.

[19] J. Xu, A. Eltaher, P. Jukes, Three-dimensional FE model for pipeline in permafrost with thermosyphon protection, in: Arctic Technology Conference, Vol. 1, Houston, 2011, pp. 535–544.

[20] B. Abdalla, C. Fan, C. Mckinnon, V. Gaffard, Numerical study of ther-

mosyphon protection for frost heave, in: ASME 2015 34th International Conference on Ocean, Vol. 5A, Newfoundland, 2015, pp. 1–6.

[21] B. A. Abdalla, H. Mei, C. McKinnon, V. Gaffard, Numerical evaluation of permafrost thawing in arctic pipelines and mitigation strategies, in: Arctic Technology Conference 2016, Newfoundland, 2016.

[22] J.-L. Wang, S.-M. Liao, Numerical heat transfer analysis and optimization for thermosyphons coupled with natural ground in permafrost regions, China Railway Science 27 (6) (2006) 1–6.

[23] Y.-H. Tian, J.-K. Liu, Y.-P. Shen, 3-D finite element analysis of cooling effect of Qinghai-Tibet Railway embankment with thermosyphons in permafrost regions, Chinese Journal of Geotechnical Engineering 35 (2013) 113–119.

[24] M. Zhang, Y. Lai, J. Zhang, Z. Sun, Numerical study on cooling characteristics of two-phase closed thermosyphon embankment in permafrost regions, Cold Regions Science and Technology 65 (2) (2011) 203–210.

[25] H. Imura, H. Kusuda, J.-I. Ogata, T. Miyazaki, N. Sakamoto, Heat transfer in two-phase closed-type thermosyphons, JSME Transactions 45 (1979) 712–722.

[26] Y. Mu, G. Li, Q. Yu, W. Ma, D. Wang, F. Wang, Numerical study of long-term cooling effects of thermosyphons around tower footings in permafrost regions along the Qinghai-Tibet Power Transmission Line, Cold Regions Science and Technology 121 (2016) 237–249.

[27] M. Zhang, W. Pei, Y. Lai, F. Niu, S. Li, Numerical study of the thermal characteristics of a shallow tunnel section with a two-phase closed thermosyphon group in a permafrost region under climate warming, International Journal of Heat and Mass Transfer 104 (2017) 952–963.

[28] W. Pei, M. Zhang, S. Li, Y. Lai, L. Jin, W. Zhai, F. Yu, J. Lu, Geotemperature control performance of two-phase closed thermosyphons in the shady and sunny slopes of an embankment in a permafrost region, Applied Thermal Engineering 112 (2017) 986–998.

[29] L. Chen, W. Yu, Y. Lu, W. Liu, Numerical simulation on the performance of thermosyphon adopted to mitigate thaw settlement of embankment in sandy permafrost zone, Applied Thermal Engineering 128 (2018) 1624–1633.

[30] H. Yandong, W. Qingbai, D. Jianhua, L. Jing, Z. Mingli, Y. Zeguo, Numerical simulation of efficient cooling by coupled RR and TCPT on railway embankments in permafrost regions, Applied Thermal Engineering 133 (2018) 351–360.

[31] W. Pei, M. Zhang, Z. Yan, S. Li, Y. Lai, Numerical evaluation of the cooling performance of a composite L-shaped two-phase closed thermosyphon (LTPCT) technique in permafrost regions, Solar Energy 177 (2019) 22–31.

[32] W. Pei, M. Zhang, Y. Lai, Z. Yan, S. Li, Evaluation of the ground heat control capacity of a novel air-L-shaped TPCT-ground (ALTG) cooling system in cold regions, Energy 179 (2019) 655–668.

[33] Y. Lai, H. Guo, Y. Dong, Laboratory investigation on the cooling effect of the embankment with L-shaped thermosyphon and crushed-rock revetment in permafrost regions, Cold Regions Science and Technology 58 (3) (2009) 143–150.

[34] Y. Song, L. Jin, J. Zhang, In-situ study on cooling characteristics of two-phase closed thermosyphon embankment of Qinghai-Tibet Highway in permafrost regions, Cold Regions Science and Technology 93 (2013) 12–19.

[35] S. Wang, L. Jin, H. Peng, J. Chen, K. Mu, Damage analysis of the characteristics and development process of thermosyphon embankment along the Qinghai-Tibet Highway, Cold Regions Science and Technology 142 (2017) 118–131.

[36] J. Wu, W. Ma, Z. Sun, Z. Wen, In-situ study on cooling effect of the two-phase closed thermosyphon and insulation combinational embankment of the Qinghai-Tibet Railway, Cold Regions Science and Technology 60 (3).

[37] M. Zhang, Y. Lai, Y. Dong, L. Jin, W. Pei, J. Harbor, Laboratory investigation of the heat transfer characteristics of a two-phase closed thermosyphon, Cold Regions Science and Technology 95 (2013) 67–73.

[38] M. A. Alzoubi, M. Xu, F. P. Hassani, S. Poncet, A. P. Sasmito, Artificial ground freezing: A review of thermal and hydraulic aspects, Tunnelling and Underground Space Technology 104 (2020) 103534.

[39] A. Zueter, A. Nie-Rouquette, M. A. Alzoubi, A. P. Sasmito, Thermal and hydraulic analysis of selective artificial ground freezing using air insulation: Experiment and modeling, Computers and Geotechnics 120 (2020) 103416.

[40] M. A. Alzoubi, A. Zueter, A. Nie-Rouquette, A. P. Sasmito, Freezing on demand: A new concept for mine safety and energy savings in wet underground mines, International Journal of Mining Science and Technology 29 (4) (2019) 621–627.

[41] M. Xu, S. Akhtar, A. Zueter, V. Auger, M. Alzoubi, A. P. Sasmito, Development of analytical solution for a two-phase Stefan problem in artificial ground freezing using singular perturbation theory, Journal of Heat Transfer. 142 (12) (2020) 122401.

[42] M. A. Alzoubi, A. P. Sasmito, Thermal performance optimization of a bayonet tube heat exchanger, Applied Thermal Engineering 111 (2017) 232–247.

[43] D. F. Haynes, J. P. Zarling, W. F. Quinn, G. E. Gooch, Laboratory tests with a hybrid thermosyphon, in: Proceedings of the 10th International Conference on Ocean, Offshore and Arctic Engineering, Vol. 4, American Society of Mechanical Engineers, Stavanger, 1991, pp. 93–99.

[44] A. M. Wagner, Creation of an artificial frozen barrier using hybrid thermosyphons, Cold Regions Science and Technology 96 (2013) 108–116.

[45] A. M. Wagner, E. Yarmak, The performance of artificial frozen barriers, in: ISCORD 2013: Planning for Sustainable Cold Regions, 2013, pp. 116–127.

[46] SRK Consulting (Canada) Inc., Freeze Optimization Study Update for MVEIRB and Parties Aboriginal Affairs and Northern Development Freeze Optimization Study Update for MVEIRB and Parties, Tech. Rep. August, Ottawa (2012).

[47] M. Kaviany, Principles of Heat Transfer in Porous Media, Springer Science & Business Media, 2012.

[48] Y. A. Cengel, Heat and Mass Transfer: Fundamentals and Applications, 3rd Edition, McGraw-Hill, Boston, 2007.

[49] J. Gao, Y. Lai, M. Zhang, D. Chang, The thermal effect of heating two-phase closed thermosyphons on the high-speed railway embankment in seasonally frozen regions, Applied Thermal Engineering 141 (2018) 948–957.

[50] V. Guichet, S. Almahmoud, H. Jouhara, Nucleate pool boiling heat transfer in wickless heat pipes (two-phase closed thermosyphons): A critical review of correlations, Thermal Science and Engineering Progress 13 (2019) 100384.

[51] W. Nusselt, The condensation of steam on cooled surfaces, Z. Ver. Dtsch. Ing 60 (1916) 541–546.

[52] V. Guichet, H. Jouhara, Condensation, evaporation and boiling of falling films in wickless heat pipes (two-phase closed thermosyphons): A critical review of correlations, International Journal of Thermofluids 1 (2020) 100001.

[53] A. Zukauskas, Heat Transfer from Tubes in Crossflow, in: Advances in heat transfer, Vol. 8, Elsevier, 1972, pp. 93–160.

[54] K. A. Gardner, Efficiency of extended surface, Transactions of ASME 67 (1945) 621–631.

[55] X. Wang, H. Yao, J. Li, Y. Wang, Y. Zhu, Experimental and numerical investigation on heat transfer characteristics of ammonia thermosyhpons at shallow geothermal temperature, International Journal of Heat and Mass Transfer 136 (2019) 1147–1159.

[56] B. K. Hardik, P. K. Baburajan, S. V. Prabhu, Local heat transfer coefficient in helical coils with single phase flow, International Journal of Heat and Mass Transfer 89 (2015) 522–538.

[57] R. A. Seban, E. F. McLaughlin, Heat transfer in tube coils with laminar and turbulent flow, International journal of heat and mass transfer 6 (5) (1963) 387–395.

[58] C. M. White, Streamline flow through curved pipes, Proceedings of the Royal Society of London. Series A, Containing Papers of a Mathematical and Physical Character 123 (792) (1929) 645–663.

[59] W. Pei, M. Zhang, S. Li, Y. Lai, Y. Dong, L. Jin, Laboratory investigation of the efficiency optimization of an inclined two-phase closed thermosyphon in ambient cool energy utilization, Renewable Energy 133 (2019) 1178–1187.

[60] M. Noel, D. Hockley, Thermal analysis of an experimental thermosyphon installed at the Giant Mine in Yellowknife, NT, Canada, in: 57th Canadian Geotechnical Conference and 5th joint CGS-IAH Conference, Quebec, 2004.

[61] M. Fong, M. A. Alzoubi, J. C. Kurnia, A. P. Sasmito, On the performance of ground coupled seasonal thermal energy storage for heating and cooling: A Canadian context, Applied Energy 250 (2019) 593–604.

[62] Government of Canada, Historical Data (2019).
URL `https://climate.weather.gc.ca/`

[63] J. Zhou, W. Zhao, Y. Tang, Practical prediction method on frost heave of soft clay in artificial ground freezing with field experiment, Tunnelling and Underground Space Technology 107 (2021) 103647.

[64] N/A, 2009 ASHRAE handbook : fundamentals, inch-pound Edition, American Society of Heating, Refrigerating and Air-Conditioning Engineers, Inc. (ASHRAE), Atlanta, GA., 2009.

[65] National Institute of Standards and Technology, NIST chemistry webbook (2018).
URL `https://webbook.nist.gov/`

property	value
Finned area of passive condenser	39 [m^2]
Evaporator outer diameter	73 [mm]
Evaporator thickness	5.3 [mm]
Condenser outer diameter	88.9 [mm]
Condenser thickness	8 [mm]

Table 1: Geometry of the test thermosyphon used in the passive model validation. Details on the geometry can be found in [60].

Material	ρ [kg/m^3]	c_p [J/(kg·k)]	k [W/(m·k)]	μ [Pa s]
Condensate CO_2 [65]	959	2396	0.117	1.09E-4
Vapor CO_2 [65]	81.9	1643	18.0E-2	1.42E-5
R-507 [64]	1263	1279	89.1E-2	2.61E-4
Frozen overburden [3]	1867	1158	2.09	-
Unfrozen overburden [3]	1900	1564	1.40	-
Frozen rock-1 [3]	2958	784	2.61	-
Unfrozen rock-1 [3]	2959	792	2.59	-
Frozen rock-2 [46]	2926	814	3.45	-
Unfrozen rock-2 [46]	2927	822	3.44	-

Table 2: Thermophysical properties of the materials used in the Giant Mine tests. Rock-1 and rock-2 refer to the bedrock of the passive experiment and the bedrock of the hybrid experiment, respectively. The water content is 1% of all field simulations [3, 46].

property	value
Finned area of passive condenser	39 [m^2]
Thermosyphon outer diameter	114 [mm]
Thermosyphon thickness	10 [mm]
Helical coil outer diameter	10.3 [mm]
Helical coil thickness	1.7 [mm]
Helical coil height	2.4 [m]

Table 3: Geometry of hybrid thermosyphons used in our calculations [46].

Simulation	$E(t = 1[\text{yr}])$ [MWh] active	$E(t = 1[\text{yr}])$ [MWh] passive	$E(t = 2[\text{yr}])$ [MWh] active	$E(t = 2[\text{yr}])$ [MWh] passive
Base-case	30.8	17.1	60.5	33.4
$T_c = -20[°C]$	20.7	17.4	40.5	34.4
$T_c = -40[°C]$	40.8	16.8	80.3	32.6
$\dot{m}_c = 20[\text{kg/hr}]$	25.1	17.3	49.3	34
$\dot{m}_c = 100[\text{kg/hr}]$	33.5	17.0	65.7	33.2
$\tau = 4[\text{mo.}]$	21.0	18.2	41.3	35.7
$\tau = 8[\text{mo.}]$	40.5	15.1	79.4	28.7
$R^* = 5$	13.4	17.7	26.6	35.1
$R^* = 15$	38.8	16.9	76.1	32.8
double-coil	42.2	16.8	82.6	32.5

Table 4: Active and passive energy extracted by the coolant in different simulation scenarios. The simulation parameters of the base case are $T_c = -30[°C]$, $\dot{m}_c = 60[\text{kg/hr}]$, $\tau = 6$ [months], $R^* = 10$, and a single helical coil.

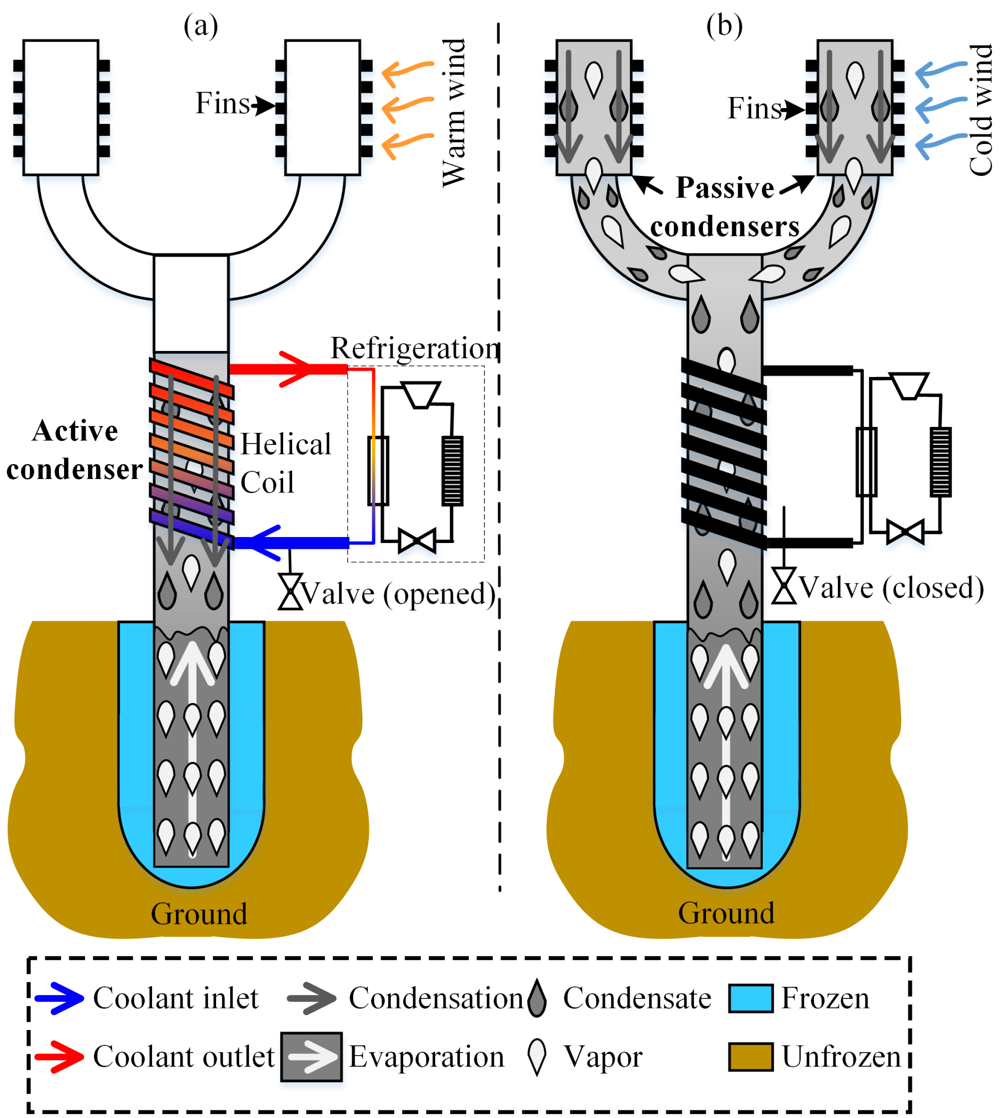

Figure 1: The operating principle of hybrid thermosyphons in artificial ground freezing applications: a) Active operation employing a refrigeration plant during warm season and b) passive operation utilizing cold air temperature during cold seasons (not-to-scale).

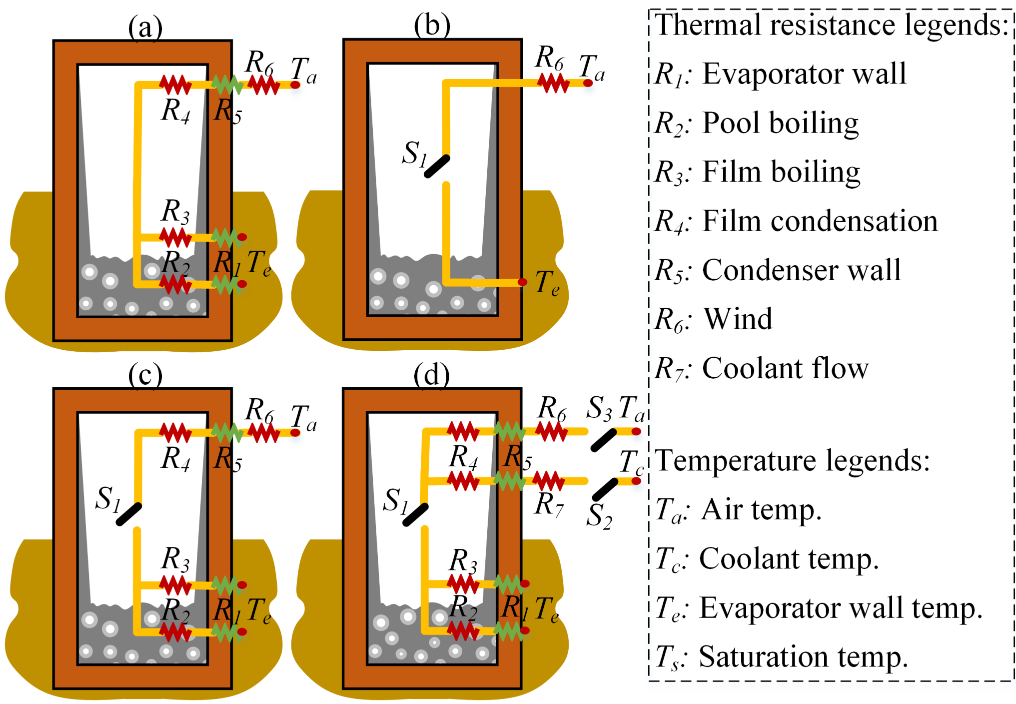

Figure 2: Progression of thermal resistance models of thermosyphons: a) The first passive cooling model developed by Yang et al. [15, 16, 17], b) passive cooling model assuming thermosyphon as a super-conductor [18, 19, 20, 21, 22, 23], c) the most widely used passive cooling model [24, 26, 27, 28, 29, 30, 31, 32], and d) hybrid cooling model of the present study (not-to-scale).

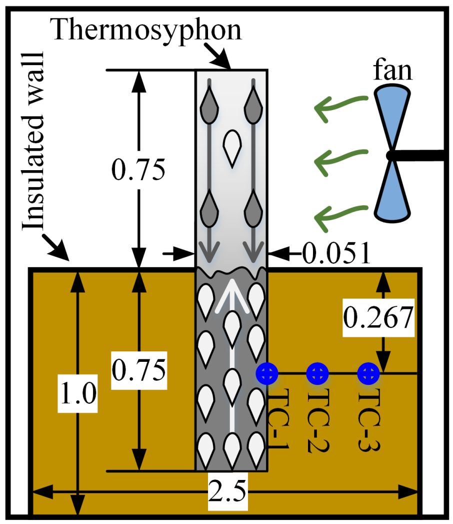

Figure 3: Non-to-scale schematic of the experimental setup of Pei et al. [59]. The blue circles indicate the thermocouples (TC) positions (please refer to Fig. 1 to find the labels of other symbols). TC-1 is fixed at the outer wall of the evaporator, while TC-2 and TC-3 are displaced 0.2 [m] and 0.5 [m] from the thermosyphon, respectively. The ground volume is 2.5 [m] × 1.84 [m] × 1.0 [m].

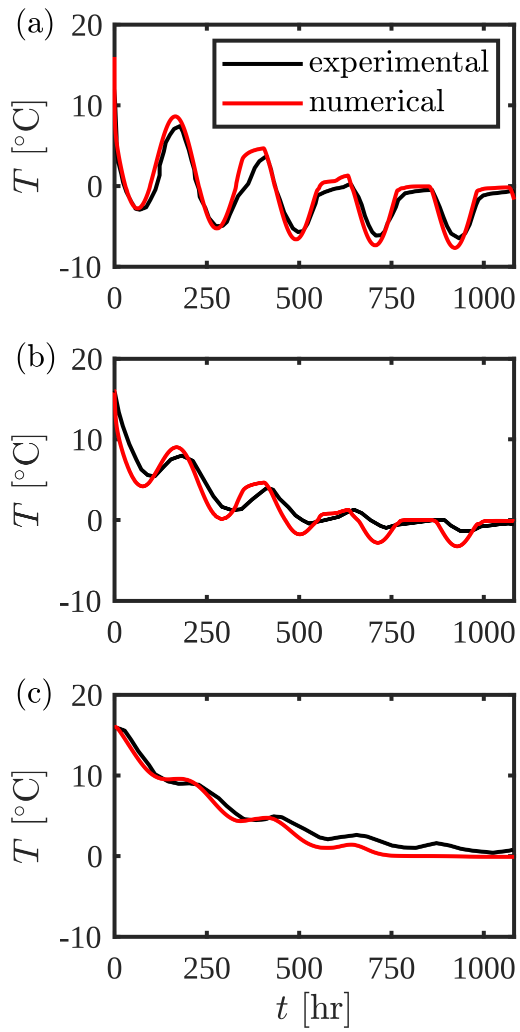

Figure 4: Validation of the present model against the experimental study of Pei et al. [59] a) At the evaporator wall (TC-1), b) horizontal distance of 0.2 [m] from the evaporator wall (TC-2), and c) horizontal distance of 0.5 [m] from the evaporator wall (TC-3). The position of the thermocouples is shown in Fig. 3.

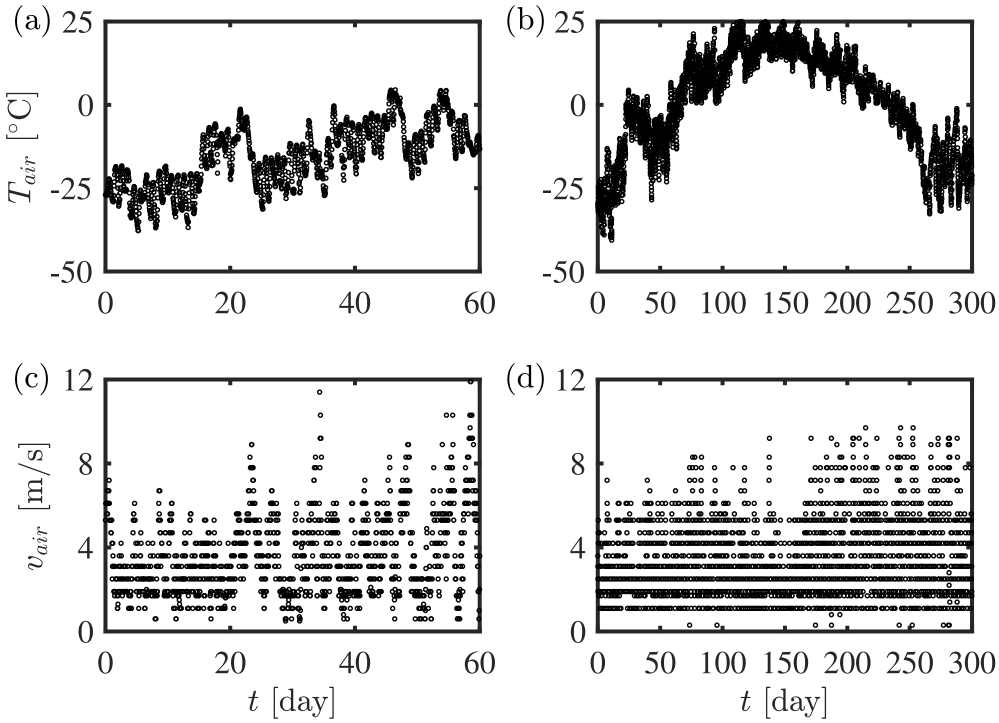

Figure 5: Hourly air data measured by the Giant Mine weather station [62]: Air temperature data of the a) passive thermosyphon test and b) hybrid thermosyphon test, and air speed data of the c) passive thermosyphon test and d) hybrid thermosyphon test.

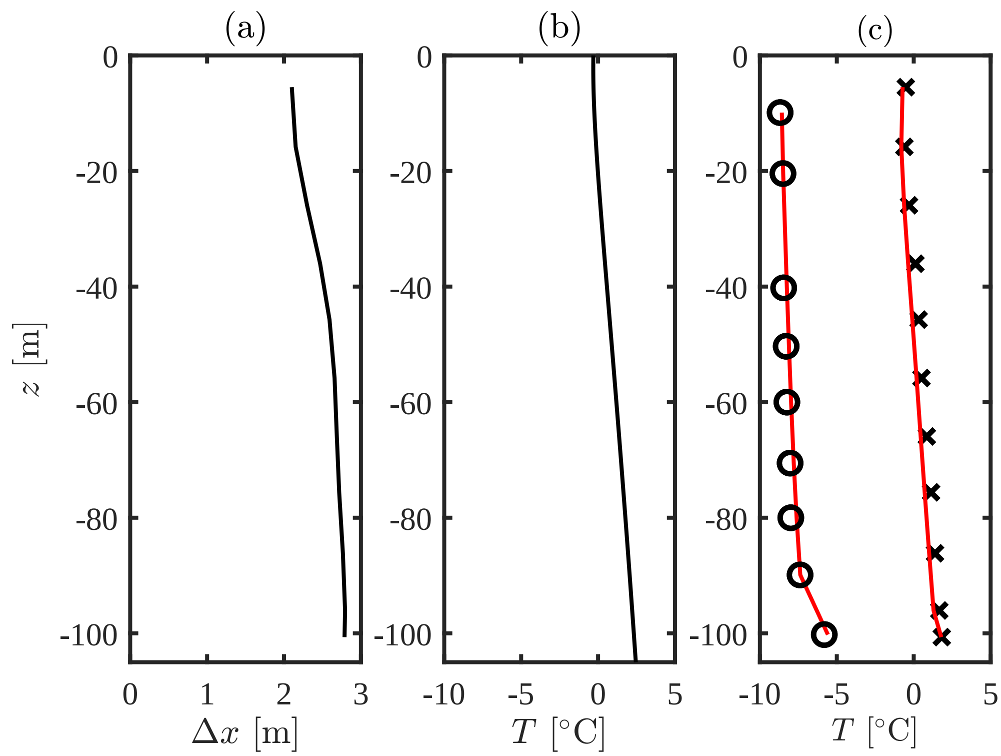

Figure 6: Validation of the passive cooling model of the present study against the Giant Mine field test [3]: a) Displacement of the instrumentation hole from the thermosyphon, b) Initial ground temperature as measured by the thermocouples and then curve-fitted, and c) validation of our mathematical model (red line) against the experimental measurements of the temperature on the thermosyphon wall (o) and in the instrumentation hole (×).

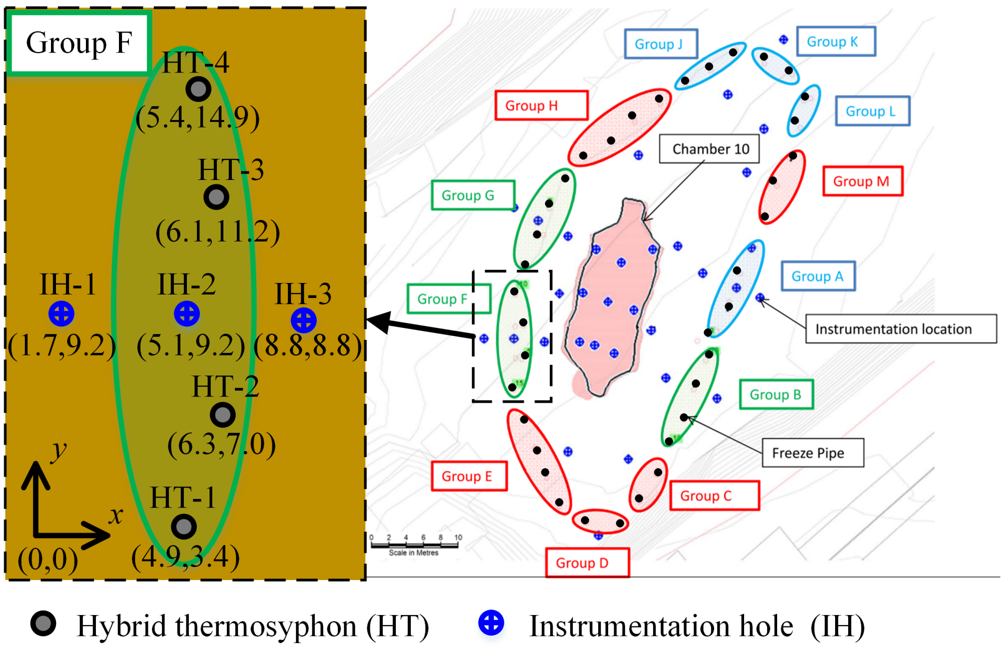

Figure 7: Freeze optimization study (FOS) of the Giant Mine surrounding one of the arsenic chambers included 12 different groups to compare between various AGF techniques [46]. In this study, group F is selected which involves four hybrid thermosyphons (HT) and three instrumentation holes (IH). Non-to-scale coordinates of each HT and IH are provided in the zoomed figure with respect to an arbitrary reference point.

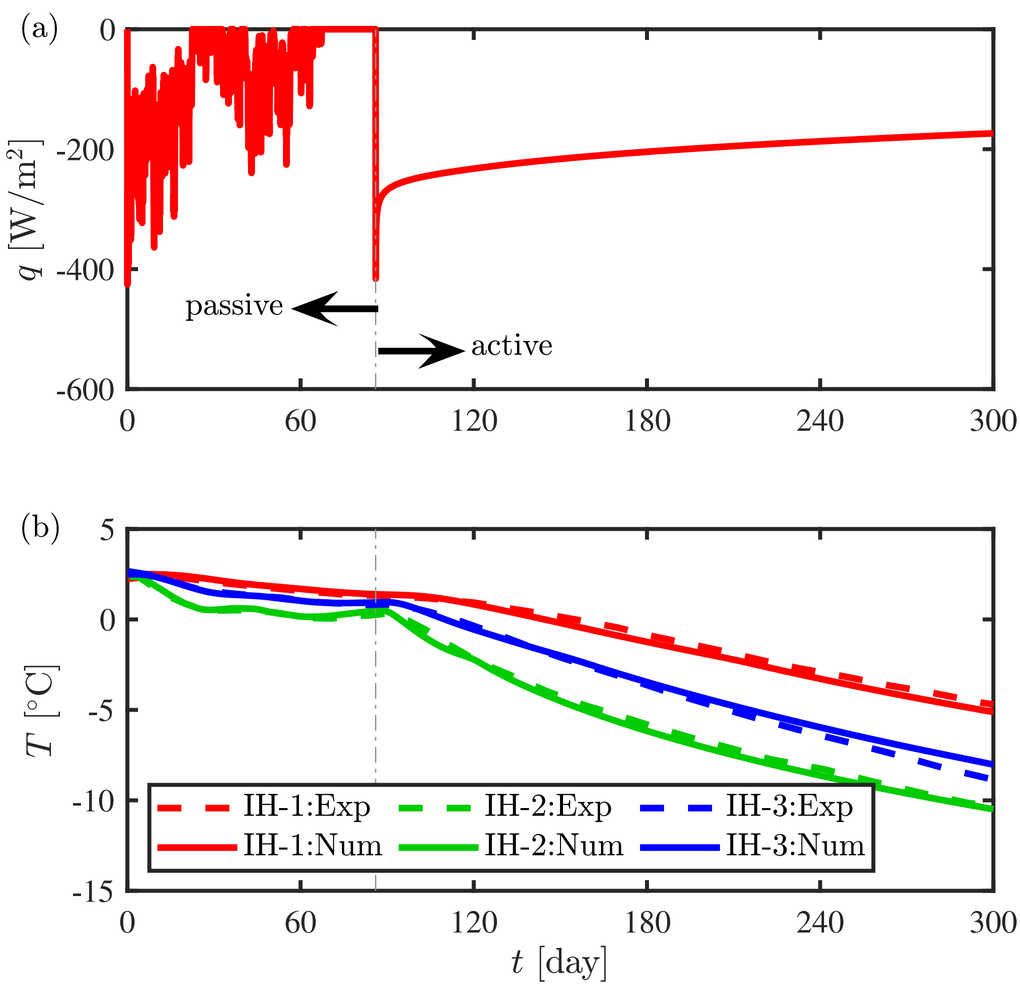

Figure 8: Mathematical modeling results of the Giant Mine Field tests [46]: a) Averaged heat flux extracted by the four hybrid themrosyphons during passive and active operations and b) validation of the hybrid model of the present study against the temperature measurements recorded by three different instrumentation holes (IH), shown in Fig. 7. The heat flux of each thermosyphon is calculated based on the heat-flux boundary condition coupling the ground with the thermosyphons (Eq. (17)). The calculated heat flux of each thermosyphon was found to be almost identical due to their identical operational parameters although there are very small differences because of their different spatial positions.

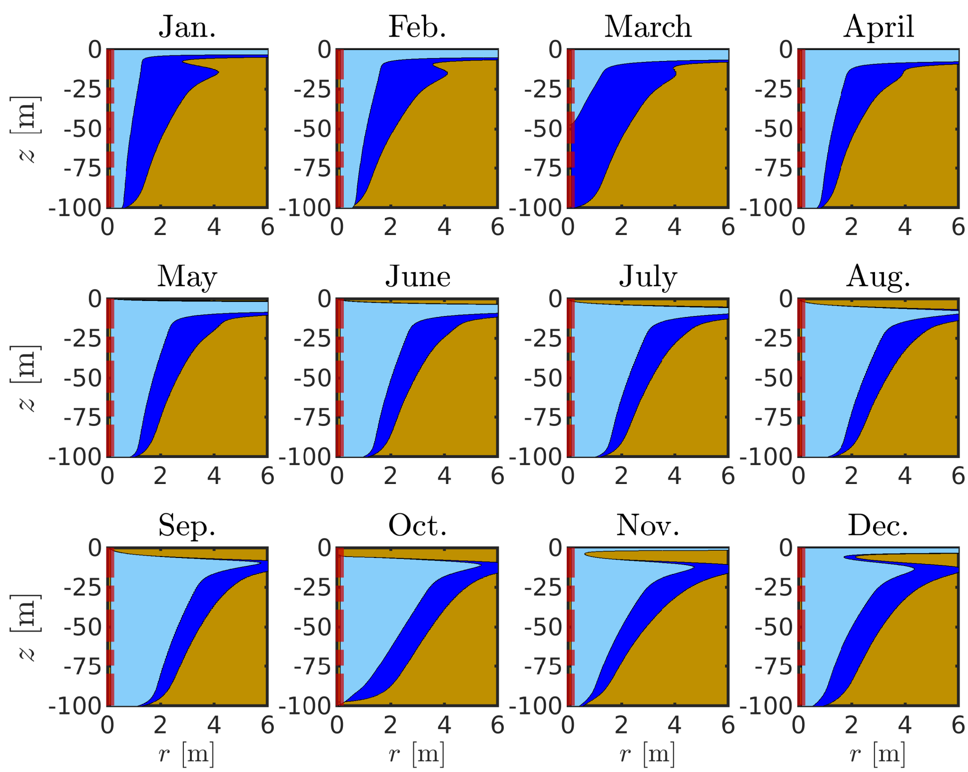

Figure 9: Monthly deformation of the frozen ground throughout the operation of a single hybrid thermosyphon for a period of two years. The dashed line represents the axis of symmetry of the thermosyphon and the computational domain. Light blue corresponds to the frozen ground in the first year of each month, while dark blue shows the increased frozen ground volume in the second year of the same month. The operational parameters are: $T_c = -30$[°C], $\dot{m}_c = 60$[kg/hr], and $\tau = 6$ [months], whereas the geometry of helical coil is given in Table 3. The results are plotted at the end of each month.

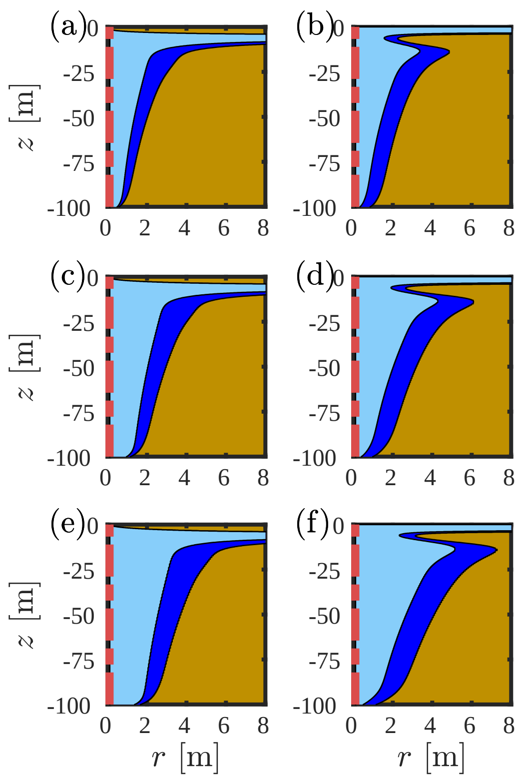

Figure 10: The effect of coolant temperature on the frozen ground volume during summer seasons (1st of July) and winter seasons (31st of December): a) $T_c = -20$ [°C] - summer, b) $T_c = -20$ [°C] - winter c) $T_c = -30$ [°C] - summer, d) $T_c = -30$ [°C] - winter, e) $T_c = -40$ [°C] - summer, f) $T_c = -40$ [°C] - winter. Other operational parameters and description of the figure colors can be found in the caption of Fig. 9.

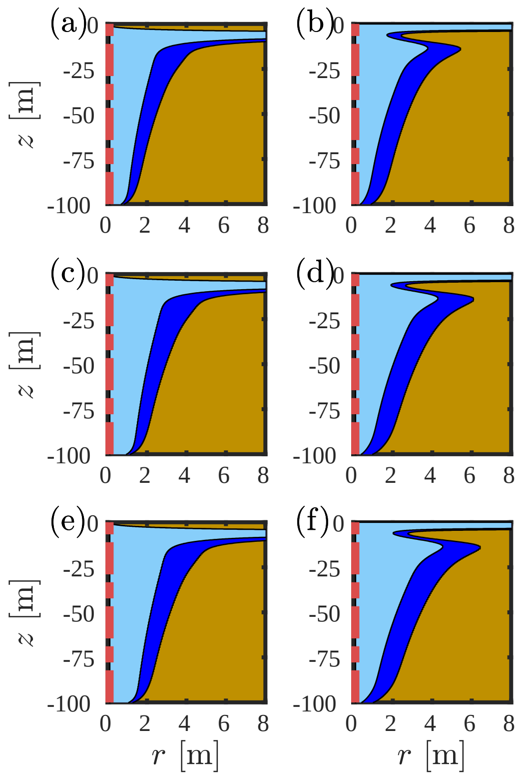

Figure 11: The effect of coolant flow rate on the frozen ground volume during summer seasons (1st of July) and winter seasons (31st of December): a) $\dot{m}_c$ = 20 [kg/hr] - summer, b) $\dot{m}_c$ = 20 [kg/hr] - winter c) $\dot{m}_c$ = 60 [kg/hr] - summer, d) $\dot{m}_c$ = 60 [kg/hr] - winter, e) $\dot{m}_c$ = 100 [kg/hr] - summer, f) $\dot{m}_c$ = 100 [kg/hr] - winter. Other operational parameters and description of the figure colors can be found in the caption of Fig. 9.

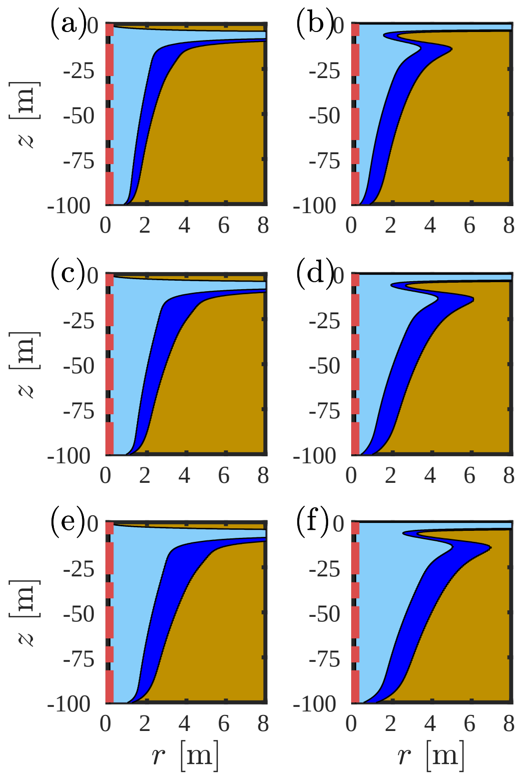

Figure 12: the effect of active cooling operational period per year, τ, on the frozen ground volume during summer seasons (1st of July) and winter seasons (31st of December): a) τ = 4 [months] - summer, b) τ = 4 [months] - winter c) τ = 6 [months] - summer, d) τ = 6 [months] - winter, e) τ = 8 [months] - summer, f) τ = 8 [months] - winter. Other operational parameters and description of the figure colors can be found in Fig. 9.

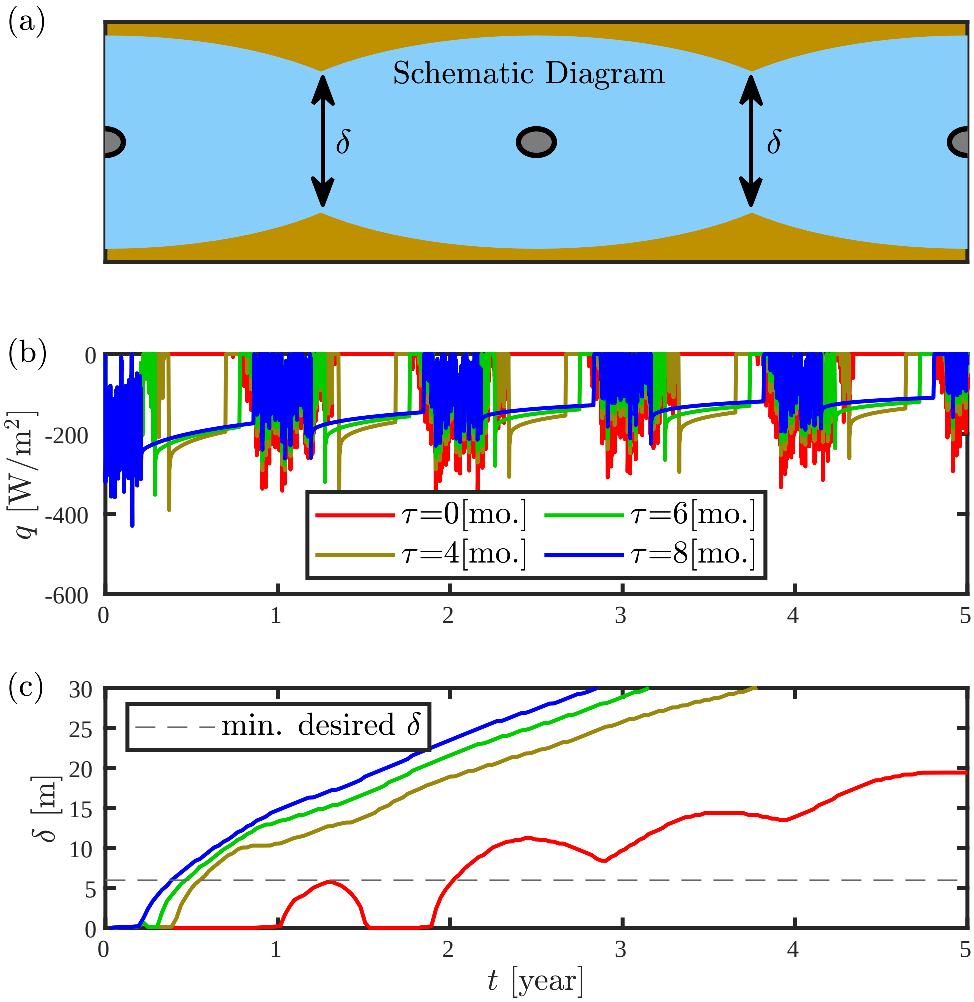

Figure 13: Thermal analysis on the influence of active cooling operational period per year, τ, when multiple thermosyphons are adjacent to each other. a) A non-to-scale schematic illustrating the lateral thickness of the frozen ground, δ. The gray circles represent thermosyphons while blue and brown colors indicate frozen and unfrozen ground. b) Transient heat flux extracted by the thermosyphons, and c) transient lateral ground thickness at different τ (τ = 0 indicates a fully passive operation). All the results plotted in this figure and Fig. 14 are obtained by simulating multiple thermosyphons in a straight row as shown in sub-figure (a).

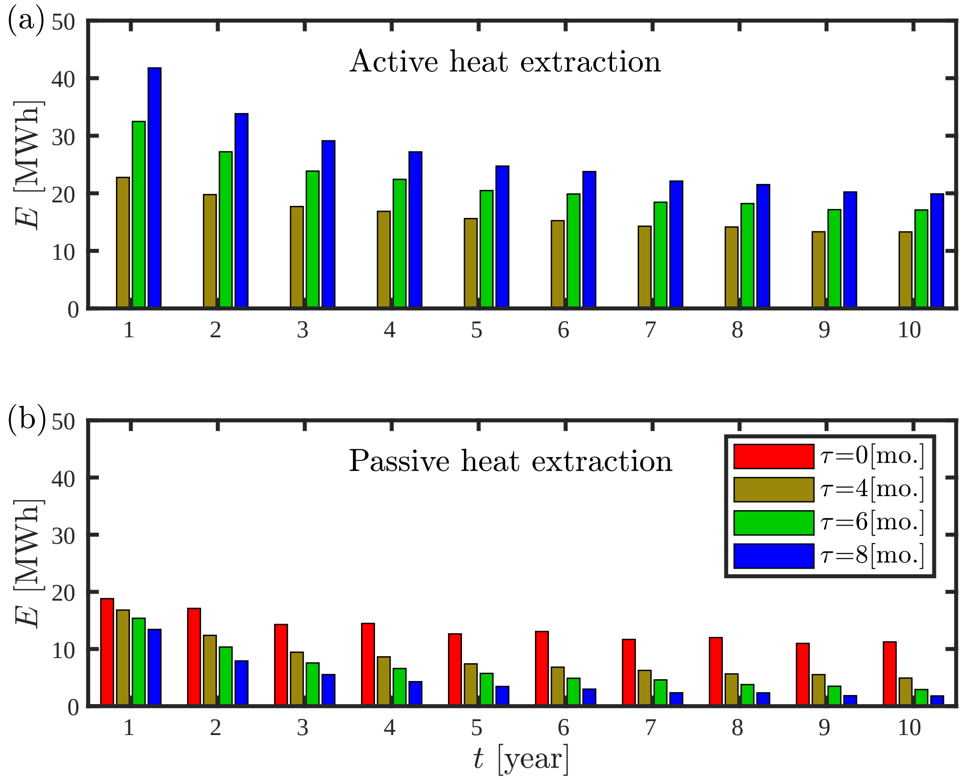

Figure 14: Influence of active operation period per year, τ, on the a) active, and b) passive heat extraction from the ground by every thermosyphon when multiple thermosyphons are working together as shown in Fig. 13(a) (τ = 0 indicates a fully passive operation).

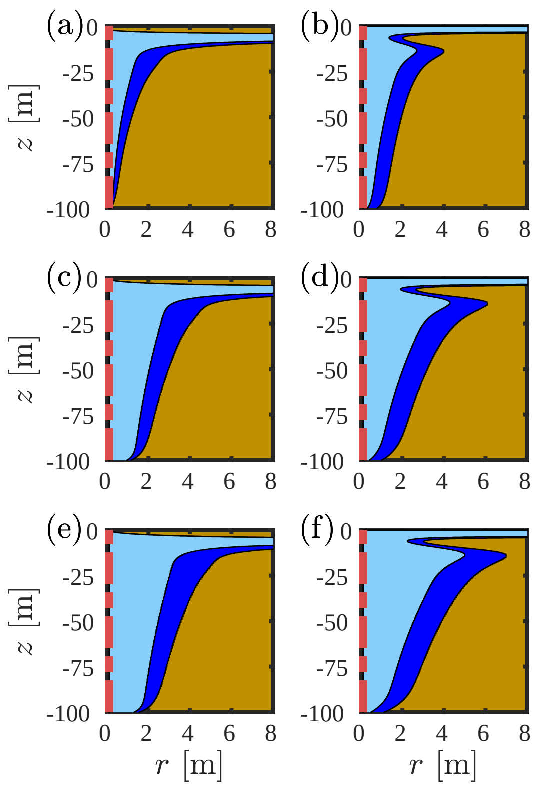

Figure 15: The effect of the curvature ratio of the helical coil, R^*, on the frozen ground volume during summer seasons (1st of July) and winter seasons (31st of December): a) R^*=5 - summer, b) R^*=5 - winter c) R^*=10 - summer, d) R^*=10 - winter, e) R^*=15 - summer, f) R^*=15 - winter. Other operational parameters and description of the figure colors can be found in the caption of Fig. 9.

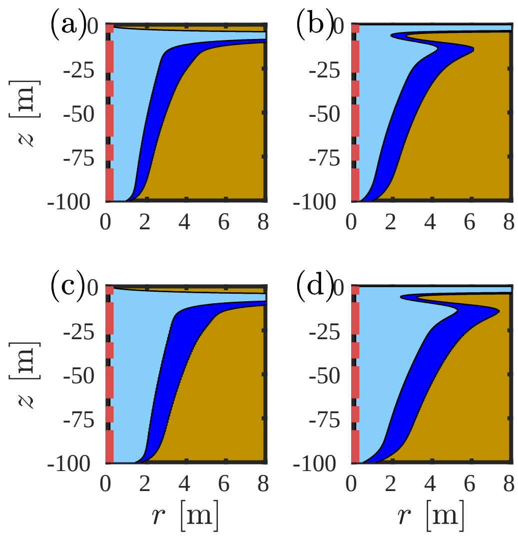

Figure 16: The effect of the number of helical coils on the frozen ground volume during summer seasons (1st of July) and winter seasons (31st of December): a) single coil - summer, b) single coil - winter c) double coil - summer, d) double coil - winter. Other operational parameters and description of the figure colors can be found in the caption of Fig. 9.